Optics Letters

Monolithically integrated dual-channel coherent receiver with widely tunable local oscillator for 100 Gbps dual-polarization quadrature phase shift keying applications

Phillip J. Skahan,[1,*] Sarat Gundavarapu,[1] Kimchau N. Nguyen,[2] Douglas M. Baney,[3] and Daniel J. Blumenthal[1]

[1]Electrical and Computer Engineering Department, University of California, Santa Barbara, California 93106, USA
[2]Intel Corporation, 2200 Mission College Blvd., SC-12, MS 326, Santa Clara, California 95054, USA
[3]Keysight Laboratories, Keysight Technologies, 5301 Stevens Creek Blvd., Santa Clara, California 95051, USA
*Corresponding author: pskahan@ece.ucsb.edu

Received 13 May 2015; revised 22 August 2015; accepted 22 August 2015; posted 24 August 2015 (Doc. ID 239933); published 11 September 2015

We report implementation of a monolithically integrated 100 Gbps dual-polarization quadrature phase shift keying (DP-QPSK) wavelength tunable coherent receiver on a 1 mm × 3 mm die that consists of a tunable C-Band local oscillator with a 40 nm range, eight 30 GHz photodetectors, and two parallel 90° optical hybrids. A BER of 10^{-3} with an OSNR of 7.5 dB operating at 50 Gbps NRZ-QPSK data per channel is reported.

OCIS codes: (060.2330) Fiber optics communications; (060.1660) Coherent communications; (130.3120) Integrated optics devices.

http://dx.doi.org/10.1364/OL.40.004313

Coherent data transmission is used to increase the spectral efficiency of existing fiber optic transmission systems and improve tolerance to transmission impairments. As the industry moves toward reducing transceiver costs to below $1/Gb, monolithic integration of the system components is beneficial for cost, size, and power reduction, especially considering the increased component count and complexity of the transmitters and receivers required for higher-order modulation formats. In the case of the receiver, there are strict tolerances on insertion losses, optical and electrical signal-to-noise ratio, and received signal phase control. Differences in the quadrature angle of the incoming signal phase at the photodetectors will result in received signal degradation and an increased bit error rate. By integrating all optical paths on-chip, path length differences may be tightly controlled and phase error minimized. On-chip integration of the local oscillator (LO) also minimizes optical loss, thus reducing power requirements on the tunable lasers and resulting in improved link sensitivity, reduced physical footprint, and reduced system complexity.

Demonstrations of monolithic coherent receivers on InP to date include on- or off-chip polarization splitters and rotators, 90° optical hybrids, and balanced photodetectors [1–7]. These designs use an external laser source as the LO. Another example has implemented an array of static distributed feedback lasers and receivers for wavelength division multiplexing applications [8]. One recent example implemented a second regrowth to integrate both the LO and high-speed photodetectors, at the cost of increased process complexity [9]. Two receiver examples integrate an LO with a single- or dual-channel coherent receiver but were RC limited by parasitic capacitance in the photodetector electrical pads and did not come close to utilizing available performance in the quantum-well diodes [10,11].

The monolithically integrated receiver reported here utilizes an improved photodiode contact design, which consists of a thicker low-κ dielectric material beneath the contacts and reduced contact surface area. This results in photodiodes limited by electron transit time through the absorption layer rather than the external RF path. These contacts have remained capable of wire bonding and showed an improved 3 dB RF response of over 30 GHz, including wire bond and coplanar transmission line network. A single on-chip LO signal split between the two channels reduces system complexity and cost, and the fabrication process requires only a single regrowth step to define the quantum wells used for gain and absorption.

A system-level schematic of the receiver is shown in Fig. 1(a). The receiver consists of two parallel 90° optical hybrids, eight single-ended photodetectors, a sampled-grating distributed Bragg reflector (SG-DBR) laser, and connecting waveguides. The hybrids consist of four four-port multimode interferometer (MMI) splitters designed to split the incoming optical signal 50/50 into each output port, similar to [12]. The MMIs were designed to operate over a 100 nm range from 1500 to 1600 nm. The first set of MMIs split the data and LO signals, and one output port from each MMI is routed to each of the second set of MMIs, which mix the data and LO signal; the unused input ports on the hybrids were terminated with absorbing regions to minimize reflections. The LO path to the lower MMI is tuned 90° out of phase with respect to

0146-9592/15/184313-04$15/0$15.00

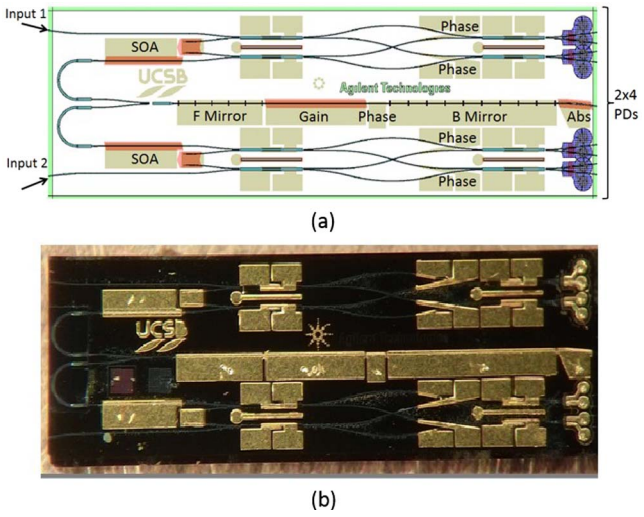

Fig. 1. (a) Operation schematic of the integrated tunable coherent receiver with LO and (b) photograph of the fabricated device. PIC measures 1.0 mm × 2.975 mm.

the upper LO path using an electro-optic phase shifter, thus producing the quadrature data. The optical signals are then detected in waveguide photodiodes downstream of the MMI outputs; the diodes are single-ended due to a shared n-type substrate ground. The SG-DBR laser consists of a front mirror, back mirror, and phase section with electro-optic phase shifters, a gain section, and an absorber section. The laser is designed with a Bragg wavelength $\lambda_B = 1540$ nm, and the peak spacing is 3.55 and 3.24 nm for the front and back mirrors, respectively. The output of the laser is TE-polarized due to tensile strain on the quantum wells in the gain section. The LO output is split by a 1 × 2 MMI and routed to each optical hybrid. A photograph of the fabricated device is shown in Fig. 1(b).

The receiver was fabricated on a semiconducting InP substrate. The epitaxial structure consists of a quaternary waveguide layer with a 1.4 μm bandgap, a multiple quantum well gain/absorption layer, and a regrown InP upper cladding. The fabrication process consists of eight mask layers and one regrowth. All features except the waveguide gratings were defined using an i-line stepper; the gratings were defined using electron beam lithography. Novel steps in the device fabrication include use of benzocyclobutene (BCB) under the metal contacts of the photodetectors, reduced photodiode contact surface area, and an inductively coupled plasma (ICP) dry etch for the waveguides. A schematic of the fabricated photodetector is shown in Fig. 2. The photosensitive BCB was spun at low revolutions per minute, resulting in a 7.5 μm thick layer after curing. The metal contacts were defined 14 μm around the waveguides with a 60 μm diameter circular pad at one end for wire bonding; total pad surface area is ∼4000 μm^2. Waveguides were etched into the semiconductor material with an ICP dry etch consisting of chlorine, nitrogen, and argon gas. Line edge roughness of the resulting waveguides was measured to be 20 nm root mean square, which is sufficient for propagation losses lower than 2 dB/mm. The fabricated device was thinned to 150 μm, cleaved, and soldered to an AlN carrier for improved thermal stability.

The LO was first tested to determine the range of operation, output power, and side mode suppression ratio (SMSR). Tuning range was determined by sweeping the front and back

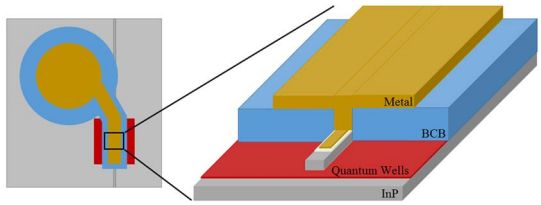

Fig. 2. 3D model of the waveguide photodetector.

mirror currents from 0 to 40 mA and measuring the output wavelength of the device in an optical spectrum analyzer (OSA); the results of this measurement are plotted in Fig. 3. Typical observed SMSR was >48 dB, with quasi-continuous tuning shown over a 44 nm range from 1520 to 1564 nm. Threshold current was 34 mA. Next, the photodiodes were swept with an optical signal from 100 MHz to 40 GHz using a Keysight lightwave component analyzer to determine RF performance; a normalized response from one of the photodiodes biased at −2 V is presented in Fig. 4, displaying a 30 GHz 3 dB optical bandwidth. All electrical connections up to the coplanar waveguide (CPW) transmission lines were calibrated out of the measurement; the wire bonds and CPW lines were included. Several dips in the response magnitude were due to resonances from ground discontinuities on the CPW lines. Photodiode dark current was 10–15 μA across all photodiodes with laser and phase sections biased. Resistivity of the diodes was roughly 3000 $\Omega \cdot \mu m^2$ measured with on-chip transmission line

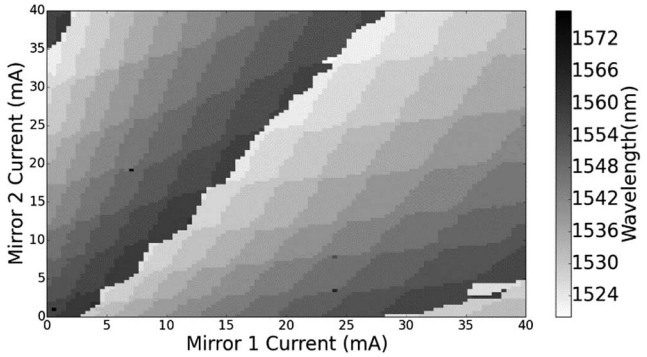

Fig. 3. Measured SG-DBR wavelength versus current.

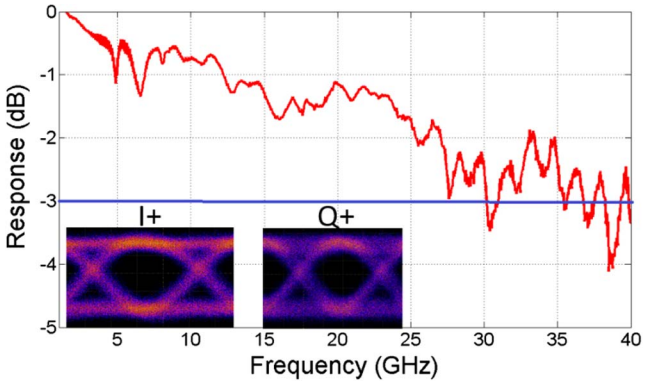

Fig. 4. Measured optical-electrical frequency response of the photodiode.

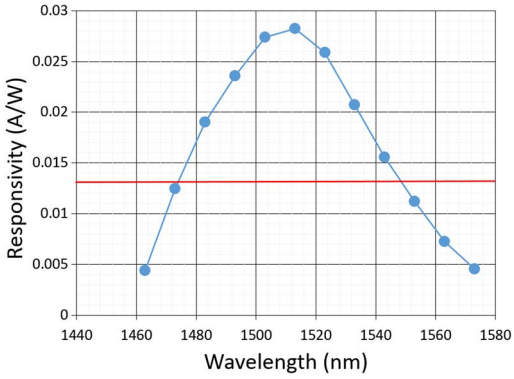

Fig. 5. Measured net receiver responsivity versus wavelength.

method structures; this resulted in the 30 × 3.65 μm photodiodes typically having a resistance of about 27 Ω. Responsivity of the photodiode was 0.3 A/W measured with an off-chip test structure; the measurement includes coupling loss from a lensed fiber with a 2.5 μm spot size to the on-chip waveguide. Net receiver responsivity was measured and is plotted versus wavelength in Fig. 5 for a −1.5 V bias on the photodiodes; the maximum net responsivity was 0.03 A/W at 1513 nm. Useful optical bandwidth of the receiver is over 100 nm. Net responsivity includes 6 dB splitting loss in the hybrid and the responsivity of the photodiodes; thus, the excess loss of the receiver is 4.1 dB or roughly 1.4 dB/mm waveguide loss due to photon scattering from line edge roughness and inter-valence band absorption in the upper cladding layer.

To verify photodiode operation, an amplitude-shift keyed nonreturn-to-zero (NRZ) pseudorandom binary sequence (PRBS) with a pattern length of $2^7 - 1$ at 25 GHz was fed into the device and recovered at the positive in-phase (I+) and quadrature (Q+) photodiodes. The optical signal was preamplified to 20 dBm using an erbium-doped fiber amplifier (EDFA) and filtered using a 0.4 nm tunable filter before being coupled into the chip, and the received photocurrent was amplified with an RF amplifier, similar to the setup shown in Fig. 6. Open eyes from both photodiodes are shown as inserts in Fig. 4.

The available LO power was determined by biasing the laser at 191 mA and measuring the photocurrent in the diodes; the LO photocurrents were in the range of 200–300 μA across the photodiodes. The linewidth of the LO was then measured using the self-heterodyne method. The output from the back of the LO was coupled off-chip using a lensed fiber and then split in a 50/50 fiber coupler. One output was delayed with a 20 km length of LEAF fiber, and the other output was shifted 100 MHz using an acousto-optic modulator. The beams were then combined in another 50/50 fiber coupler, converted to an electrical current through a high-speed photodiode, and measured in an electrical spectrum analyzer with a 200 kHz resolution bandwidth. Linewidths (3 dB) of 12, 15, and 18 MHz were measured at 1545.26, 1548.38, and 1551.5 nm, respectively; these wavelengths were achieved by tuning only the front mirror of the laser. The increasing trend in linewidth is likely due to increased electro-optic absorption in the mirrors, as each higher wavelength required a 2–3 mA increase in the current to the front mirror. To eliminate reflections from the back facet, which could cause injection locking of the SG-DBR, the absorber section of the laser was reverse biased. At the front

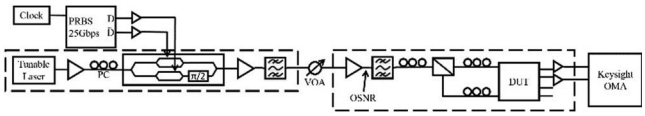

Fig. 6. Schematic of the setup used for receiver characterization.

of the laser, reflections from the hybrids back into the LO were minimal due to 8 dB of path loss through the waveguide bends, resulting in 16 dB total return loss. An external cavity laser with a 100 kHz linewidth was coupled with the on-chip LO using the on-chip hybrid, and the RF spectrum of the resulting beat frequency was measured from one of the photodiodes. The 3 dB linewidth of the beat tone was 130 MHz, which is much larger than the linewidth of the individual lasers, due to significant 1/f noise of the two lasers from thermal fluctuations and vibrations. The beat frequencies detected in the I+ and Q+ photodetectors were then viewed simultaneously with a real-time oscilloscope, and the phase path of the lower half of each hybrid was tuned so that the beat frequencies were 90° out of phase, thus ensuring quadrature encoded data recovery. A 50 Gbps NRZ quadrature phase-shift keyed (QPSK) signal generated from two individual PRBS $2^7 - 1$ data streams was used to test individual channel operation; the test setup is shown in Fig. 6.

A polarizing beam splitter cube was used before the receiver inputs to separate incoming polarization-multiplexed signals; the transverse-electric (TE) path was fed directly to one channel, while the transverse magnetic (TM) signal was rotated to the TE orientation using a polarization controller before being fed to the other channel for compatibility with the LO signal. The optical signal was again preamplified to 20 dBm using an EDFA and filtered with a 0.4 nm tunable filter before being coupled into the chip, and the received photocurrents were amplified with an RF amplifier and processed using a Keysight optical modulation analyzer (OMA). The OMA contains a digital signal processor (DSP), which performed equalization, clock recovery, carrier phase estimation, decoding, and error detection. Three different wavelengths were tested to verify receiver operation, and the resulting bit-error rate (BER) versus the optical signal-to-noise ratio (OSNR) of the input signal is presented in Fig. 7.

An error floor was measured at 10^{-8} for all three wavelengths, likely due to the 130 MHz linewidth of the beat tone. A BER of 10^{-3} was achieved at an OSNR of 7.5 dB for the 1548.38 and 1551.5 nm wavelengths, while an OSNR of 11.5 dB was required to achieve the same BER at 1545.26 nm. This difference can be attributed to the carrier phase estimation algorithm implemented in the DSP, which uses a Kalman filter to compensate for the phase noise of the beat tone and determine the phase of the signal. At 1545.26 nm, the LO linewidth was narrow enough that the phase estimation could be set low, resulting in less phase distortion of the recovered signal, as shown in the recovered constellation in Fig. 8. At 1548.38 and 1551.5 nm, the linewidths required more aggressive phase estimation, resulting in increased phase distortion of the recovered constellations. A secondary effect was an improvement in the measured BER versus OSNR at these wavelengths, as the phase estimation likely caused minor error correction of some of the errors from noise in the incoming signal, resulting in a measured BER exceeding the theoretical limit for a nonerror-corrected signal at the lower OSNR points.

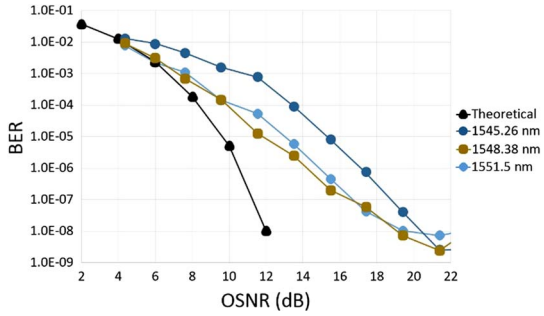

Fig. 7. Measured BER versus OSNR for 50 Gbps NRZ-QPSK data into a single channel.

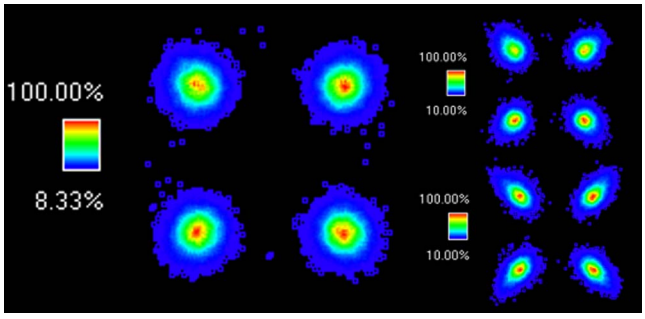

Fig. 8. Recovered constellations at three different wavelengths for 50 Gbps NRZ-QPSK data into a single channel: 1545.26 nm, left; 1548.38 nm, top right; 1551.5 nm, bottom right.

In conclusion, we demonstrated a monolithically integrated dual-channel heterodyne receiver with a widely tunable local oscillator for application in 100 Gbps optical networks utilizing coherent modulation formats. The receiver consists of a tunable C-band local oscillator with a 40 nm range, eight 30 GHz photodetectors, and two parallel 90° optical hybrids integrated on a 1 mm × 3 mm die. We found that the improved photodiode design consisting of a thicker low-κ dielectric material beneath the contacts and a reduced contact surface area resulted in devices limited by electron transit time through the absorption layer rather than the external RF path. The contacts for these devices remained capable of wire bonding and showed an improved 3 dB response of over 30 GHz, including the wire bond and coplanar transmission line network. Only a single regrowth step was required to define the quantum wells used for gain and absorption, minimizing process complexity. The on-chip LO signal split between the two channels resulted in reduced system complexity, cost, and improved link sensitivity with no observed instability due to on-chip reflections, which is likely due to 16 dB return loss through the LO output path. We measured an LO linewidth of 12–18 MHz at three different wavelengths and found that the linewidth was correlated to current injection of the tuning mirror. Using 50 Gbps NRZ-QPSK data per channel, we demonstrated a BER of 10^{-3} at an OSNR of 7.5 dB at three different wavelengths, and we observed an error floor at a BER of 10^{-8} caused by the 130 MHz linewidth of the beat tone. Future directions for this work include linewidth reduction of the LO and optical phase locking to enable higher-modulation formats. Thermally tuned SG-DBR lasers have been demonstrated with 200–300 kHz linewidths over a 40 nm tuning range by eliminating the current injection in the mirror sections [13], and electronic feedback from an asymmetric Mach–Zehnder has been used to reduce an SG-DBR laser linewidth from 19 MHz down to 570 kHz [14] with theoretical capability below 100 kHz. Additionally, integrated optical phase locking would eliminate the low frequency drift between the carrier and LO and has been demonstrated on a heterodyne receiver with an integrated SG-DBR [15]. Other work includes on-chip integration of polarization splitting and electrical amplifier functions to further reduce system complexity, use of total internal reflection mirrors on the LO path to increase available LO power in the photodiodes, and a directional coupler-based 90° optical hybrid to minimize injection locking of the LO due to reflections.

Funding. Keysight Technologies.

REFERENCES

1. H. Bach, A. Matiss, C. Leonhardt, R. Kunkel, D. Schmidt, M. Schell, and A. Umbach, in *Optical Fiber Communication Conference*, Technical Digest (Optical Society of America, 2009), paper OMK5.
2. A. Beling, N. Ebel, A. Matiss, G. Unterbörsch, M. Nölle, J. Fischer, J. Hilt, L. Molle, C. Schubert, F. Verluise, and L. Fulop, in *Optical Fiber Communication Conference*, Technical Digest (Optical Society of America, 2011), paper OML5.
3. A. Matiss, R. Ludwig, J. Fischer, L. Molle, C. Schubert, C. Leonhardt, H. Bach, R. Kunkel, and A. Umbach, in *Optical Fiber Communication Conference*, Technical Digest (Optical Society of America, 2010), paper PDPB3.
4. C. R. Doerr, L. Zhang, and P. J. Winzer, IEEE J. Lightwave Technol. **29**, 536 (2011).
5. C. R. Doerr, L. Zhang, P. J. Winzer, N. Weimann, V. Houtsma, T. Hu, N. J. Sauer, L. L. Buhl, D. T. Neilson, S. Chandrasekhar, and Y. K. Chen, IEEE Photon. Technol. Lett. **23**, 694 (2011).
6. M. Boudreau, M. Poirier, G. Yoffe, and B. Pezeshki, in *Optical Fiber Communication Conference*, Technical Digest (Optical Society of America, 2009), paper OMK6.
7. V. Houtsma, N. Weimann, T. Hu, R. Kopf, A. Tate, J. Frackoviak, R. Reyes, Y. Chen, C. Doerr, L. Zhang, and D. Neilson, in *Optical Fiber Communication Conference*, Technical Digest (Optical Society of America, 2011), paper OML2.
8. R. Nagarajan, D. Lambert, M. Kato, V. Lal, G. Goldfarb, J. Rahn, M. Kuntz, J. Pleumeekers, A. Dentai, H. Tsai, R. Malendevich, M. Missey, K. Wu, H. Sun, J. McNicol, J. Tang, J. Zhang, T. Butrie, A. Nilsson, M. Reffle, F. Kish, and D. Welch, in *Optical Fiber Communication Conference*, Technical Digest (Optical Society of America, 2011), paper OML7.
9. M. Lu, H. Park, A. Sivananthan, J. S. Parker, E. Block, L. A. Johanssen, M. J. W. Rodwell, and L. A. Coldren, IEEE Photon. Technol. Lett. **25**, 1077 (2013).
10. S. B. Estrella, L. A. Johansson, M. L. Masanovic, J. A. Thomas, and J. S. Barton, IEEE Photon. Technol. Lett. **24**, 365 (2012).
11. K. N. Nguyen, P. J. Skahan, J. M. Garcia, E. Lively, H. N. Poulsen, D. M. Baney, and D. J. Blumenthal, Opt. Express **19**, B716 (2011).
12. D. Hoffman, H. Heidrich, G. Wenke, R. Langenhorst, and E. Dietrich, IEEE J. Lightwave Technol. **7**, 794 (1989).
13. M. C. Larson, Y. Feng, P. C. Koh, X. Huang, M. Moewe, A. Semakov, A. Patwardhan, E. Chiu, A. Bhardwaj, K. Chan, J. Lu, S. Bajwa, and K. Duncan, in *Optical Fiber Communication Conference*, Technical Digest (Optical Society of America, 2013), paper OTh3I.4.
14. A. Sivananthan, H. Park, M. Lu, J. S. Parker, E. Bloch, L. A. Johansson, M. Rodwell, and L. Coldren, in *CLEO*, Technical Digest (Optical Society of America, 2013), paper CTu1L.2.
15. M. Lu, H. Park, E. Bloch, A. Sivananthan, A. Bhardwaj, Z. Griffith, L. A. Johansson, M. J. Rodwell, and L. A. Coldren, Opt. Express **20**, 9736 (2012).